ACS APPLIED MATERIALS & INTERFACES
RESEARCH ARTICLE
www.acsami.org

Electrodeposition of Hierarchical ZnO Nanorod-Nanosheet Structures and Their Applications in Dye-Sensitized Solar Cells

Jianhang Qiu,[†] Min Guo,[‡] and Xidong Wang*[,†]

[†]Department of Energy and Resources Engineering, Peking University, Beijing 100871, People's Republic of China
[‡]Department of Physical Chemistry, University of Science and Technology Beijing, Beijing 100083, People's Republic of China

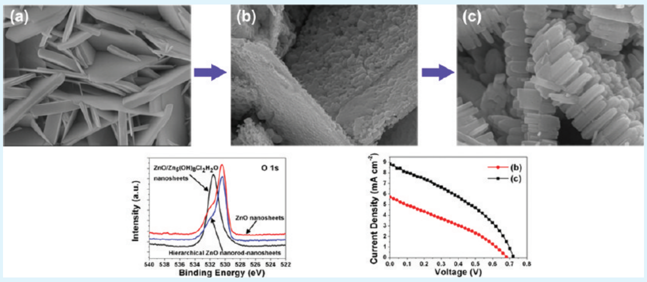

ABSTRACT: We present a two-step electrochemical deposition process to synthesize hierarchical zinc oxide (ZnO) nanorod-nanosheet structures on indium tin oxide (ITO) substrate, which involves electrodeposition of ZnO nanosheet arrays on the conductive glass substrate, followed by electrochemical growth of secondary ZnO nanorods on the backbone of the primary ZnO nanosheets. The formation mechanism of the hierarchical nanostructure is discussed. It is demonstrated that annealing treatment of the primary nanosheets synthesized by the first-step deposition process plays a key role in synthesizing the hierarchical nanostructure. Photovoltaic properties of dye-sensitized solar cells (DSSCs) based on hierarchical ZnO nanostructures are investigated. The hierarchical ZnO nanorod-nanosheet DSSC exhibits improved device performance compared to the DSSC constructed using photoelectrode of bare ZnO nanosheet arrays. The improvement can be attributed to the enhanced dye loading, which is caused by the enlargement of internal surface area within the nanostructure photoelectrode. Furthermore, we perform a parametric study to determine the optimum geometric dimensions of the hierarchical ZnO nanorod-nanosheet photoelectrode through adjusting the preparation conditions of the first- and second-step deposition process. By utilizing a hierarchical nanostructure photoelectrode with film thickness of about 7 μm, the DSSC with an open-circuit voltage of 0.74 V and an overall power conversion efficiency of 3.12% is successfully obtained.

KEYWORDS: hierarchical nanostructure, ZnO, crystal growth, electrodeposition, dye-sensitized solar cell

1. INTRODUCTION

Dye-sensitized solar cells (DSSCs) have been regarded as promising devices for energy applications because of their advantages of low cost, ease of manufacture, and use of low toxicity materials.[1,2] The photoelectrode in DSSC, which is based on mesoporous wide-band gap semiconductor nanocrystalline films sensitized by a monolayer of dye molecules, represents the heart of the device. A very important feature provided by the mesoporous nanocrystalline films is the high internal surface area (1000−2000 times the area of a flat/smooth electrode), which ensures sufficient dye loading for the photoelectrode and thus good light harvesting efficiency for the cell. To date, the DSSC with power conversion efficiency over 11% has been achieved with 20 nm titanium dioxide (TiO_2) nanocrystalline film sensitized by ruthenium-based dyes.[3,4] Nevertheless, the present benchmark power conversion efficiency obtained by researchers is still too low in comparison to the theoretical value (32%) predicted for a single junction cell.[5] It has been demonstrated that the trap-detrap diffusion process of electron transport in mesoporous nanocrystalline film, mainly caused by the defects in the nanocrystalline film, is a major limiting factor for achieving higher power conversion efficiency.[6−9] Replacing the mesoporous nanocrystalline films with one-dimensional (1D) zinc oxide (ZnO) nanostructures, such as nanowire arrays[10] or nanotube arrays,[11] is considered to be an effective way to tackle this issue, not only because 1D ZnO nanostructures can afford a direct conduction pathway for the photogenerated electron, but also because they exhibit much more higher electronic mobility (200−1000 $cm^2\ V^{-1}\ s^{-1}$) than TiO_2 nanostructures (0.1−4.0 $cm^2\ V^{-1}\ s^{-1}$), which would be favorable for rapid electron transport in photoelectrode with reduced recombination loss.[12−14] The power conversion efficiencies of the 1D ZnO nanostructure-based devices, however, are restricted to a relatively low level by the low light harvesting efficiency, which is the result of low internal surface area provided by 1D nanostructure photoelectrodes. Thus hierarchical ZnO nanostructures combining multiscale configurations, such as dendritic nanowires,[15,16] tetrapod-like nanostructures,[17] nanoflower structures,[18] and nanowire-nanosheet architectures,[19] are introduced, aimed at enlarging internal surface area of the photoelectrode while keeping high electron transport efficiency. For example, Jiang et al. fabricated a hierarchical ZnO nanoflower DSSC with a power conversion efficiency of 1.9% via hydrothermal approach, which is the highest efficiency in ZnO nanowire-based DSSCs.[18] Cheng et al. also reported a hierarchical branched ZnO nanowire photoelectrode by hydrothermal method, which exhibited an improved efficiency of 1.5% compared to the DSSC fabricated

Received: March 5, 2011
Accepted: June 15, 2011
Published: June 15, 2011

with 1D ZnO nanowires.[20] Xu et al. synthesized a hierarchical ZnO nanowire-nanosheet architectures by an electrochemical-hydrothermal process. The DSSC based on such hierarchical nanostructure exhibited a high power conversion efficiency of 4.8%, which is nearly twice as high as that of nanosheet DSSC.[19] Accordingly, hierarchical ZnO nanostructures might be a good candidate material for the photoelectrode in DSSC.

Hierarchical ZnO nanostructures can be synthesized by a variety of methods, such as chemical-vapor-deposition (CVD),[15,16,21] thermal evaporation,[22−24] hydrothermal synthesis,[18,20,25] and electrodeposition process.[26] Low-temperature process, high growth rate, ease of production on large-area substrate, and convenient operation are some of the advantages offered by electrodeposition, which are significant for further industrial applications. Electrodeposition of ZnO nanostructures is generally based on the generation of OH^- ions at the surface of working electrode by electrochemical reduction of precursors such as O_2,[27] NO_3^-,[28] and H_2O_2[29] in Zn^{2+} aqueous solution. During the deposition process, OH^- ions are produced in terms of eqs 1, 2, or 3 after certain potential is applied. Then Zn^{2+} ions in the vicinity of working electrode react with OH^- ions, resulting in formation of zinc hydroxide ($Zn(OH)_2$) (eq 4). Finally, ZnO is produced by dehydration of $Zn(OH)_2$ (eq 5).

$$O_2 + 2H_2O + 4e^- \rightarrow 4OH^- \qquad (1)$$

$$NO_3^- + H_2O + 2e^- \rightarrow NO_2^- + 2OH^- \qquad (2)$$

$$H_2O_2 + 2e^- \rightarrow 2OH^- \qquad (3)$$

$$Zn^{2+} + 2OH^- \rightarrow Zn(OH)_2 \qquad (4)$$

$$Zn(OH)_2 \rightarrow ZnO + H_2O \qquad (5)$$

The morphology of the as-synthesized ZnO nanodeposits strongly depends on the experimental conditions, particularly the Zn^{2+}concentration, which might change the reaction rate of the hydroxylation (eq 4) and dehydration (eq 5), thereby enabling modifying the growth behavior of ZnO nanodeposits.[27,30] In the electrolyte containing a low concentration of Zn^{2+}, the dehydration reaction is faster than the hydroxylation one.[27,30] Thus, $Zn(OH)_2$ can be converted into ZnO as soon as it is produced, leading to formation of 1D ZnO nanostructures (e.g., nanorods, nanowires, or nanopillars) because of the anisotropic growth along the [0001] direction of the hexagonal wurtzite structure.[27,30−35] However, the formation of ZnO produced by dehydration of $Zn(OH)_2$ could be delayed because of the relatively faster hydroxylation reaction in the case of high Zn^{2+} concentration. As a result, the growth along [0001] direction might be replaced by other preferred growth direction, such as $[01\bar{1}0]$ or $[10\bar{1}0]$,[20,36] which can give rise to formation of 2D nanostructures (e.g., nanosheets or nanowalls).[27,30] Accordingly, hierarchical ZnO nanostructures could be obtained by designing a multistep electrodeposition process, in which the Zn^{2+} concentrations in different steps are adjusted in order to obtain ZnO nanodeposits with desired morphologies.[26]

Herein we introduce a designed two-step electrodeposition process to synthesize hierarchical ZnO nanorod-nanosheet structures on indium tin oxide (ITO) substrate for application in DSSC. The two-step synthesis process consists of the electrodeposition of primary ZnO nanosheet arrays on ITO substrate and the electrochemical growth of secondary ZnO nanorods on the backbone of the primary nanosheets. The formation mechanism of the hierarchical nanostructure is discussed in detail. The DSSC based on the synthesized hierarchical nanostructure exhibits improved power conversion efficiency compared to the DSSC constructed with bare ZnO nanosheets, which can be ascribed to the enlargement of internal surface area within the photoelectrode, caused by the introduction of the secondary nanorods. We also perform a study to determine the optimum geometric dimensions of the hierarchical ZnO nanostructure photoelectrode through adjusting the preparation conditions of the two-step deposition process. By using the optimized preparation conditions, the DSSC with an open-circuit voltage of 0.74 V and an overall power conversion efficiency of 3.12% is achieved.

2. EXPERIMENTAL DETAILS

2.1. Preparation of ZnO Nanosheet Arrays and Hierarchical ZnO Nanorod-Nanosheet Structures. All reagents were analytical grade and used without further purification. All aqueous solutions were prepared using double distilled water. Electrodeposition of ZnO nanostructures was performed with an electrochemical analytical instrument (CHI 760C) in a standard three electrodes system. Pt spiral wire and saturated calomel electrode (SCE) served as counter electrode and reference electrode, respectively. Electrolytes were 0.05 M $Zn(NO_3)_2$ and 1 mM $ZnCl_2$ aqueous solution (bubbling with saturated O_2 during the reaction process) respectively for the first- and second-step deposition process and 0.1 M KCl was introduced into these two electrolytes as supporting electrolyte. The electrochemical cell was held at different temperatures and the applied potential was maintained at −1.0 V vs SCE for both the first- and second-step deposition process. Hierarchical ZnO nanorod-nanosheet structures were synthesized by a two-step electrodeposition process. First, $ZnO/Zn_5(OH)_8Cl_2H_2O$ nanosheet arrays were electrodeposited on ITO substrate (10 Ω cm^{-2}, Nippon Sheet Glass) in the electrolyte of 0.05 M $Zn(NO_3)_2$. Prior to the depositions, the ITO substrate was cleaned ultrasonically 10 min in acetone, 10 min in ethanol and then rinsed with distilled water. Second, the as-synthesized $ZnO/Zn_5(OH)_8Cl_2H_2O$ nanosheets were annealed in the air at 400 °C for 10 min to produce ZnO nanosheet arrays by decomposition of $Zn_5(OH)_8Cl_2H_2O$. Hierarchical ZnO nanorod-nanosheet structures were finally obtained by using the ZnO nanosheet arrays as working electrode for the second-step deposition process in the electrolyte of 1 mM $ZnCl_2$ (bubbling with saturated O_2).

2.2. Photoelectrochemical Measurement. The fabrication of ZnO nanostructure-based DSSCs were performed as follows: photoelectrodes of DSSCs were prepared by immersing the ZnO nanodeposits on ITO substrates into an ethanolic solution of 0.3 mM *cis*-bis(isothiocyanato)bis(2,2′-bipyridyl-4,4′-dicarboxylato)-ruthenium-(II) bis-tetrabutylammonium (N719, Solaronix) at 60 °C for 90 min. Then the samples were rinsed with ethanol to remove excess dye adsorbed. The sensitized electrodes were sandwiched together with thermally platinized FTO counter electrodes separated by about 50 μm thick spacers. The area of active electrode was 0.12 cm^2. The internal space of the two electrodes was filled with an electrolyte of 0.1 M LiI, 0.5 M 1,2-dimethyl-3-propylimidazoliumiodide, 0.03 M I_2, and 0.5 M *tert*-butylpyridine in 3-methoxypropionitrile by capillary action. The photocurrent−voltage ($J-V$) characteristics of the cells were studied using an AM 1.5 G simulated sunlight system (100 mW cm^{-2}) (Newport Corporation) with an electrochemical instrument (CHI 760C).

2.3. Characterization. The morphology and dimension of the products were characterized by scanning electron microscope (SEM; Hitachi S4800) operated at 10 kV. The crystal structure of the products was examined by X-ray diffraction (XRD; D/MAX-PC 2500 with Cu Kα

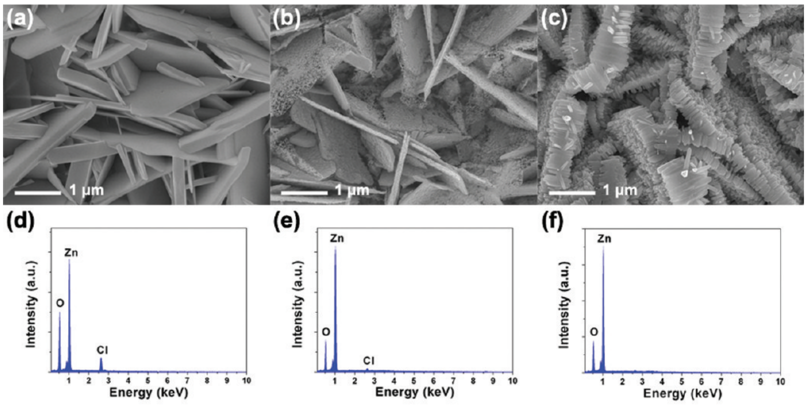

Figure 1. SEM images of ZnO nanostructures synthesized by electrodeposition process: (a) ZnO/$Zn_5(OH)_8Cl_2H_2O$ nanosheet arrays, (b) ZnO nanosheet arrays obtained by annealing the ZnO/$Zn_5(OH)_8Cl_2H_2O$ nanosheet arrays, (c) hierarchical ZnO nanorod-nanosheet structures. (d−f) Corresponding EDS spectra for (a), (b), and (c), respectively. Electrodeposition conditions of the ZnO/$Zn_5(OH)_8Cl_2H_2O$ nanosheet arrays: T = 70 °C, $C_{Zn}{}^{2+}$ = 0.05 M ($Zn(NO_3)_2$), E = −1.0 V, t = 1 h. Electrodeposition conditions of the hierarchical ZnO nanorod-nanosheet structures, first-step deposition: T_1 = 70 °C, $C_{Zn}{}^{2+}$ = 0.05 M ($Zn(NO_3)_2$), E_1 = −1.0 V, t_1 = 1 h; second-step deposition: T_2 = 80 °C, $C_{Zn}{}^{2+}$ = 1 mM ($ZnCl_2$), E_2 = −1.0 V, t_2 = 1 h.

radiation and a normal θ-2θ scan). Further structural analysis of the nanodeposits was carried out using transmission electron microscope (TEM; Tecnai F30) operated at 200 kV. The surface composition of the as-synthesized nanodeposits was analyzed by X-ray photoelectron spectroscopy (XPS; Kratos AXIS-Ultra) with a monochromatic Al Kα X-ray source (1486.7 eV). The thermal decomposition behavior of the ZnO/$Zn_5(OH)_8Cl_2H_2O$ nanodeposits synthesized by first-step deposition process was examined by thermogravimetry-differential thermal analysis (TGA-DTA-DSC; TA Instruments Q600SDT) with a heating rate of 10 °C min^{-1} in a static air atmosphere. The dye adsorption capacity of the photoelectrodes was determined as follows: the sensitized ZnO nanostructure photoelectrodes (1 cm^2) were separately immersed into a 0.1 M NaOH water−ethanol (with volume ratio of 1:1) solution (10 mL), which could result in desorption of dye molecule (N719) from the photoelectrode. The absorbance of the resulting solution was then analyzed with UV−vis spectrophotometer (XinMao UV7502PCS). The adsorbed amount of dye was determined by the molar extinction coefficient of 1.41 × 10^4 L mol^{-1} cm^{-1} at 515 nm for N719 as reported previously.[37,38]

3. RESULTS AND DISCUSSION

3.1. Preparation of Hierarchical ZnO Nanorod-Nanosheet Structures and Their Photovoltaic Properties. SEM images of ZnO nanostructures synthesized by electrodeposition approach are presented in Figure 1a-c. It can be seen from Figure 1a that sheetlike nanodeposits are produced from the electrolyte of 0.05 M $Zn(NO_3)_2$. There are diffraction features for both ZnO (JCPDS: 01−080−0074) and $Zn_5(OH)_8Cl_2H_2O$ (JCPDS: 00−007−0455) shown in XRD pattern (Figure 2a), indicating that the nanodeposits are compound of ZnO and $Zn_5(OH)_8Cl_2H_2O$. This is in agreement with the EDS spectrum (Figure 1d), in which an obvious Cl peak can be observed. The formation of $Zn_5(OH)_8Cl_2H_2O$ can be attributed to the high concentration of Zn^{2+} in electrolyte, which gives rise to the large ionic products ($[Zn^{2+}][OH^-]^2$ or $[Zn^{2+}][OH^-]^x[Cl^-]^y$) in solution and hence the precipitation of $Zn(OH)_2$ (eq 4) or zinc hydroxylchloride compounds ($Zn(OH)_xCl_y$) (eq 6) in the as-synthesized nanodeposits, as demonstrated by Peulon and co-workers.[27]

$$Zn^{2+} + xOH^- + yCl^- \rightarrow Zn(OH)_xCl_y \qquad (6)$$

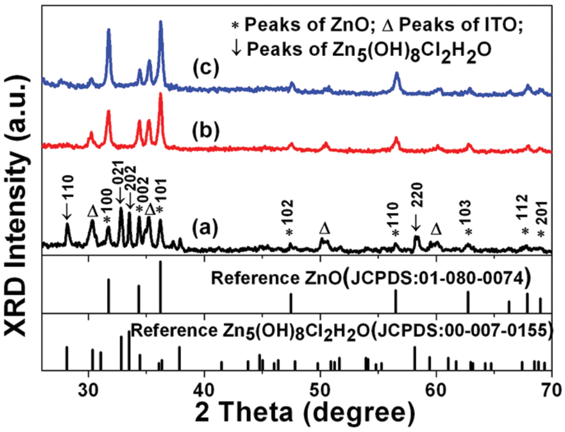

Figure 2. XRD patterns of (a) ZnO/$Zn_5(OH)_8Cl_2H_2O$ nanosheet arrays, (b) ZnO nanosheet arrays, and (c) hierarchical ZnO nanorod-nanosheet structures.

After annealing in the air at 400 °C for 10 min, the intensity of Cl peak in EDS spectrum is weakened (Figure 1e) because of the pyrolysis of $Zn_5(OH)_8Cl_2H_2O$ (eq 7).

$$Zn_5(OH)_8Cl_2H_2O \rightarrow 5ZnO + 4H_2O\uparrow + 2HCl\uparrow \qquad (7)$$

From XRD pattern shown in Figure 2b, it is clear that the ZnO/$Zn_5(OH)_8Cl_2H_2O$ nanosheets are almost converted into ZnO nanosheets. The results of XPS analysis presented in Figure 3 provide an additional evidence of this conversion. Figure 3a compares the O 1s XPS spectra of the ZnO/$Zn_5(OH)_8Cl_2H_2O$ nanosheets before and after annealing treatment, from which a shift in O 1s binding energy can be found. The higher O 1s binding energy (531.6 eV) is assigned to the hydroxyl groups located at the surface of the nanosheets,[39−42] suggesting the presence of $Zn_5(OH)_8Cl_2H_2O$ in the nanodeposits. Since the oxygen atoms in the oxide are more negatively charged than those in the M−OH species, the O 1s binding energy for ZnO nanosheets that are obtained by annealing ZnO/$Zn_5(OH)_8Cl_2H_2O$ nanosheets decreases to 530.4 eV, which agrees well to the values obtained by other researchers.[39−41,43,44] The lower O 1s binding energy for the hierarchical ZnO nanorod-nanosheets

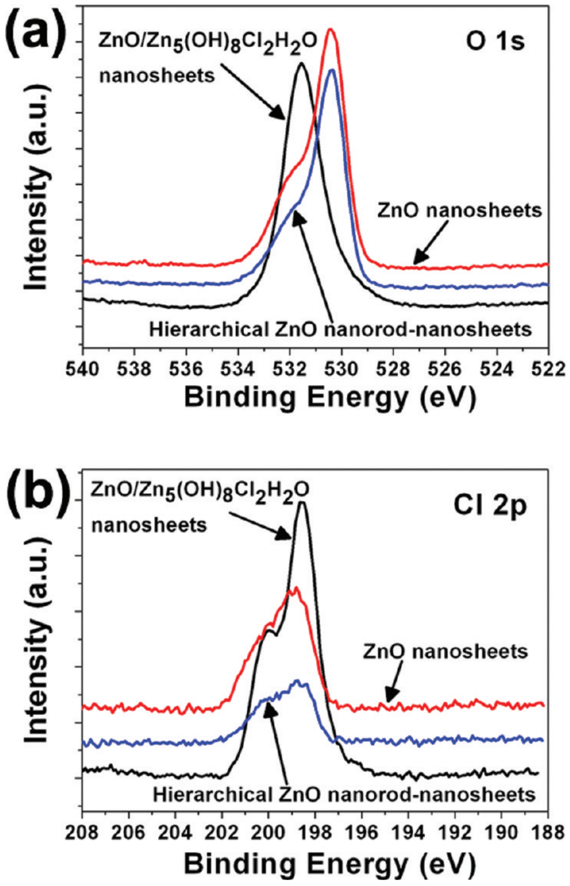

Figure 3. (a) O 1s and (b) Cl 2p XPS spectra of $ZnO/Zn_5(OH)_8Cl_2H_2O$ nanosheet arrays, ZnO nanosheet arrays, and hierarchical ZnO nanorod-nanosheet structures.

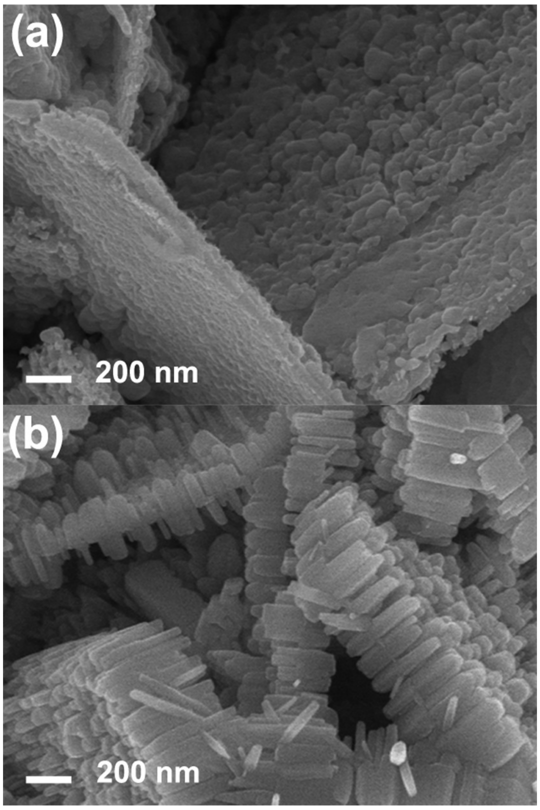

Figure 4. High-magnification SEM images of (a) ZnO nanosheets and (b) hierarchical ZnO nanorod-nanosheet structures.

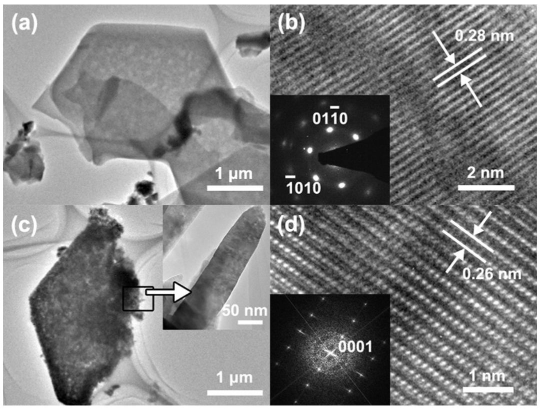

Figure 5. (a) TEM image of $ZnO/Zn_5(OH)_8Cl_2H_2O$ nanosheet, (b) HRTEM image of a section of $ZnO/Zn_5(OH)_8Cl_2H_2O$ nanosheet, the inset of (b) shows the corresponding SAED pattern of the nanosheet, (c) TEM image of the hierarchical ZnO nanorod-nanosheet structure, (d) HRTEM image of a secondary ZnO nanorod in the hierarchical nanostructure, the inset of (d) shows the corresponding SAED pattern of the nanorod.

demonstrates that the surface of the synthesized hierarchical nanostructures mainly consists of ZnO, suggesting the faster formation rate of ZnO (eq 5) in the second-step deposition process. The Cl 2p XPS spectra of the synthesized nanodeposits (Figure 3b) presents an evident variation in Cl features for the nanosheets before and after annealing treatment, which is consistent with the EDS results shown in Figure 1d and e. Moreover, because of the decomposition of $Zn_5(OH)_8Cl_2H_2O$, the original smooth surface of the nanosheets becomes rougher, with lots of asperities formed on the surface of the ZnO nanosheets (Figure 4a). These asperities possess high surface energy and hence could serve as active centers for nucleation of ZnO. During the second-step deposition process, ZnO nuclei prefer to nucleate on these active centers and then grow up into 1D nanorods because of the anisotropic growth along [0001] direction in the electrolyte containing low Zn^{2+} concentration.[27,30−35] Hierarchical ZnO nanorod-nanosheet structures are finally produced with the increase in the length of the secondary nanorods, as presented in Figures 1c and 4b.

Further structural characterizations of the as-synthesized nanodeposits were performed with TEM. Figure 5a displays a lower-magnification TEM image of the $ZnO/Zn_5(OH)_8Cl_2H_2O$ nanosheets synthesized by the first-step deposition process. The lattice spacing measured from the corresponding high revolution TEM (HRTEM) is 0.28 nm (Figure 5b), which is in good agreement with the $(01\bar{1}0)$ crystal planes of wurtzite ZnO, indicating that the nanosheets grow along the $[01\bar{1}0]$ crystallographic direction. The inset of Figure 5b shows the selected-area electron diffraction (SAED) pattern of the nanosheets, which demonstrates the crystalline nature of the nanosheets and confirms the $[01\bar{1}0]$ growth direction of the nanosheets. Figure 5c displays a TEM image of the hierarchical ZnO nanorod-nanosheet structures synthesized by the two-step deposition process, the inset of which shows a secondary ZnO nanorod in the hierarchical nanostructure. The HRTEM image

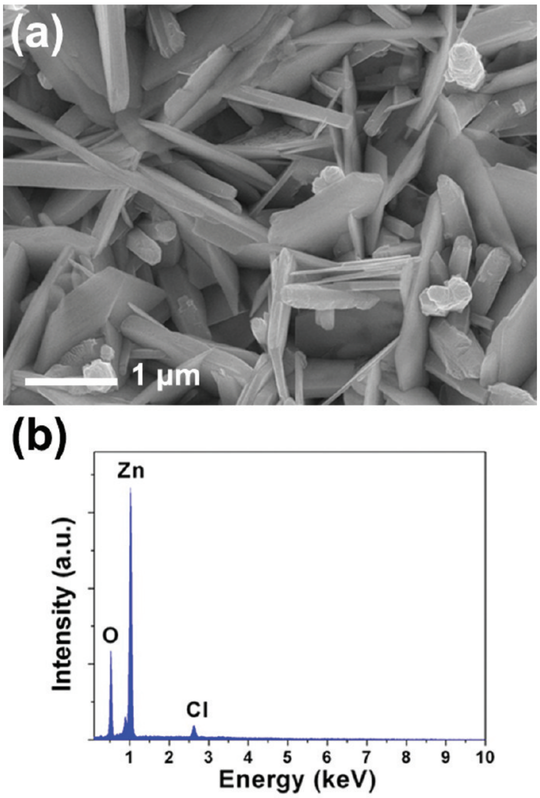

Figure 6. (a) SEM image of ZnO/$Zn_5(OH)_8Cl_2H_2O$ nanodeposits synthesized by two-step electrodeposition process in absence of annealing treatment, (b) EDS spectrum of the ZnO/$Zn_5(OH)_8Cl_2H_2O$ nanodeposits. Electrodeposition conditions of the ZnO/$Zn_5(OH)_8Cl_2H_2O$ nanodeposits, first-step deposition: $T_1 = 70\ °C$, $C_{Zn}{}^{2+} = 0.05$ M ($Zn(NO_3)_2$), $E_1 = -1.0$ V, $t_1 = 1$ h; second-step deposition: $T_2 = 80\ °C$, $C_{Zn}{}^{2+} = 1$ mM ($ZnCl_2$), $E_2 = -1.0$ V, $t_2 = 1$ h.

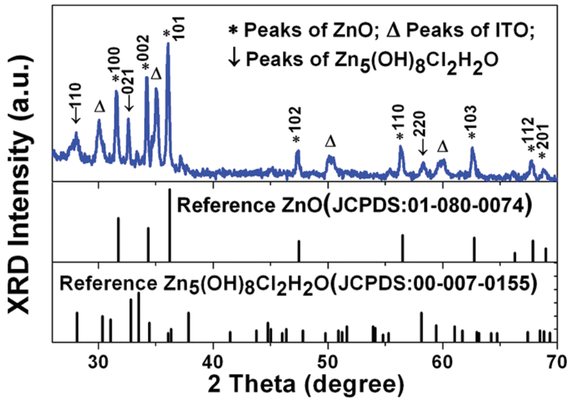

Figure 7. XRD patterns of ZnO/$Zn_5(OH)_8Cl_2H_2O$ nanodeposits synthesized by two-step electrodeposition process in absence of annealing treatment.

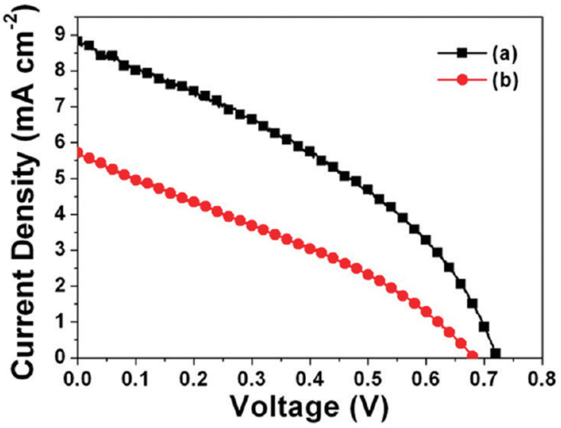

Figure 8. Photocurrent–voltage curves of DSSCs based on (a) hierarchical ZnO nanorod-nanosheet structures and (b) bare ZnO nanosheet arrays.

of the ZnO nanorod shown in Figure 5d reveals a lattice spacing of 0.26 nm, which corresponds well to the interplanar distance of the (0001) crystal planes in wurtzite ZnO, suggesting that the secondary nanorods grow along the [0001] direction. The corresponding SAED pattern (inset of Figure 5d) also demonstrates the preferred [0001] growth direction and the single-crystalline nature of the secondary nanorods.

To confirm the role of annealing treatment of the electrodeposited ZnO/$Zn_5(OH)_8Cl_2H_2O$ nanosheets in synthesizing the hierarchical nanorod-nanosheet structures, ZnO/$Zn_5(OH)_8Cl_2H_2O$ nanosheets produced by first-step deposition process was directly used as working electrode in second-step deposition process without any annealing treatment. SEM image of the resulting nanodeposits is presented in Figure 6a. It is found that no nanorod-nanosheet structures are formed after the second-step deposition process. The primary nanosheets retain their original morphology, whereas there are some ZnO nanorods with diameter of ~200 nm deposited on substrate. The corresponding EDS spectrum (Figure 6b) and XRD pattern (Figure 7) indicate that the as-synthesized nanodeposits are still composed of ZnO (JCPDS: 01–080–0074) and $Zn_5(OH)_8Cl_2H_2O$ (JCPDS: 00–007–0455). Due to the lack of active centers, which can be produced by decomposition of $Zn_5(OH)_8Cl_2H_2O$, the potential barrier for nucleation of ZnO on the surface of ZnO/$Zn_5(OH)_8Cl_2H_2O$ nanosheets is larger than that on the ITO surface. Thus ZnO nanorods prefer to originate from ITO substrate during the second-step deposition process. Consequently, no hierarchical nanorod-nanosheet structures are produced. This phenomenon demonstrates that the annealing treatment of the primary ZnO/$Zn_5(OH)_8Cl_2H_2O$ nanosheets, which allows the formation of active centers for ZnO nucleation, is crucial for synthesizing the hierarchical nanorod-nanosheet structures.

The photovoltaic properties of the DSSCs constructed with hierarchical ZnO nanorod-nanosheet structures and bare ZnO nanosheet arrays are presented in Figure 8 and Table 1. Figure 8 gives the compared photocurrent–voltage (J–V) characteristics of these two DSSCs with AM 1.5 G illumination at 100 mW cm^{-2} from a xenon lamp. The short-circuit current density (J_{sc}), the open-circuit voltage (V_{oc}), the fill factor (FF), and the overall power conversion efficiency (η) deduced from the J–V curves are summarized in Table 1. It is found that the DSSC consisting of hierarchical ZnO nanorod-nanosheet structures exhibits improved device performance, as compared to the bare ZnO nanosheet DSSC. The improvement is mainly attributed to the enlargement of internal surface area within the hierarchical nanostructure photoelectrode. From the SEM image shown in Figure 4b, it is clear that the introduction of the secondary ZnO nanorods substantially enlarges the internal surface area of the

Table 1. Photovoltaic Properties of DSSCs Based on Hierarchical ZnO Nanorod-Nanosheet Structures (sample a) and Bare ZnO Nanosheet Arrays (sample b)[a]

ZnO DSSCs	J_{sc} (mA cm^{-2})	V_{oc} (V)	FF	η (%)	amount of adsorbed dye ($\times 10^{-8}$ mol cm^{-2})
sample a	8.82	0.72	0.37	2.37	4.11
sample b	5.72	0.68	0.32	1.24	2.85

[a] The error is ±5%.Electrodeposition conditions of the ZnO nanosheet arrays: $T = 70$ °C, $C_{Zn^{2+}} = 0.05$ M ($Zn(NO_3)_2$), $E = -1.0$ V, $t = 1$ h. Electrodeposition conditions of the hierarchical ZnO nanorod-nanosheet structures, first-step deposition: $T_1 = 70$ °C, $C_{Zn^{2+}} = 0.05$ M ($Zn(NO_3)_2$), $E_1 = -1.0$ V, $t_1 = 1$ h; second-step deposition: $T_2 = 80$ °C, $C_{Zn^{2+}} = 1$ mM ($ZnCl_2$), $E_2 = -1.0$ V, $t_2 = 1$ h

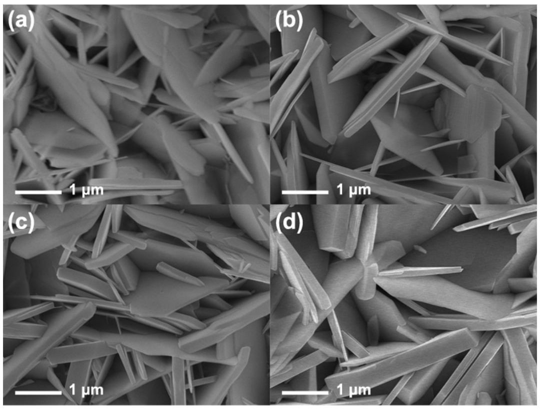

Figure 9. SEM images of $ZnO/Zn_5(OH)_8Cl_2H_2O$ nanosheet arrays electrodeposited at different temperatures (T): (a) 50, (b) 60, (c) 70, and (d) 80 °C. Other electrodeposition conditions: $C_{Zn^{2+}} = 0.05$ M ($Zn(NO_3)_2$), $E = -1.0$ V, $t = 1$ h.

hierarchical nanostructure film, resulting in enhanced dye loading of the photoelectrode (Table 1) and thus increasing the short-circuit current density from 5.72 to 8.82 mA cm^{-2}. Meanwhile, the improvements in open-circuit voltage (from 0.68 to 0.72 V) and fill factor (from 0.32 to 0.37) are achieved as well (Table 1), probably because of the formation of ZnO nanorods on the ITO surface that is not covered by the primary nanosheets, which could play a role of buffer layer and thus enabling reducing the probability of charge recombination at the interface between the ITO substrate and the electrolyte. This is in consistent with the results of Jiang et al.[18] and Cheng et al.,[20] in which the improvements in open-circuit voltage and fill factor were also obtained by the introduction of the tiny secondary nanorods on the large primary nanowire backbones. Because of the improvements in working current, open-circuit voltage and fill factor, the hierarchical nanostructure DSSC reaches an overall power conversion efficiency of 2.37%, which is almost twice as high as that of the nanosheet one (1.24%).

3.2. Influence of the Composition of $ZnO/Zn_5(OH)_8Cl_2H_2O$ Nanosheets on the Morphology of the Synthesized Hierarchical Nanostructure Photoelectrodes and Their Photovoltaic Properties. It has been demonstrated that the presence of $Zn_5(OH)_8Cl_2H_2O$ in primary $ZnO/Zn_5(OH)_8Cl_2H_2O$ nanosheets, which can give rise to the formation of active centers for ZnO nucleation by annealing treatment, plays an important role in synthesizing the hierarchical nanorod-nanosheet structures. Since the formations of ZnO (eq 4 and 5) and $Zn_5(OH)_8Cl_2H_2O$ (eq 6) strongly depend on temperature, first-step deposition temperature was adjusted to 50, 60, 70, and 80 °C, respectively, to investigate its influence on the composition of $ZnO/Zn_5(OH)_8Cl_2H_2O$ nanosheets. SEM images of the as-synthesized $ZnO/Zn_5(OH)_8Cl_2H_2O$ nanosheet arrays are presented in Figure 9. The XRD analysis (Figure 10) indicates that the composition of the as-synthesized nanodeposits varies with the temperature. The features in the XRD pattern for the nanosheets electrodeposited at 50 °C correspond well to $Zn_5(OH)_8Cl_2H_2O$ (JCPDS 00−007−0455) (Figure 10a), suggesting the large amount of $Zn_5(OH)_8Cl_2H_2O$ in the nanodeposits. This further implies that the Zn^{2+} ions in electrolyte prefer to form $Zn_5(OH)_8Cl_2H_2O$ (eq 6) because of the restriction of dehydration of $Zn(OH)_2$ (eq 5) in the case of low deposition temperature. However, the dehydration reaction is gradually enhanced with the temperature, which can result in the enhancement in the growth rate of ZnO, and thereby increasing the amount of ZnO in the synthesized nanodeposits. From the XRD patterns shown in Figure 10b, c, and d, it is found that the diffraction features of ZnO (JCPDS: 01−080−0074) are gradually enhanced with the temperature increasing from 60 to 80 °C, demonstrating the variation in amount of ZnO in the synthesized $ZnO/Zn_5(OH)_8Cl_2H_2O$ nanodeposits.

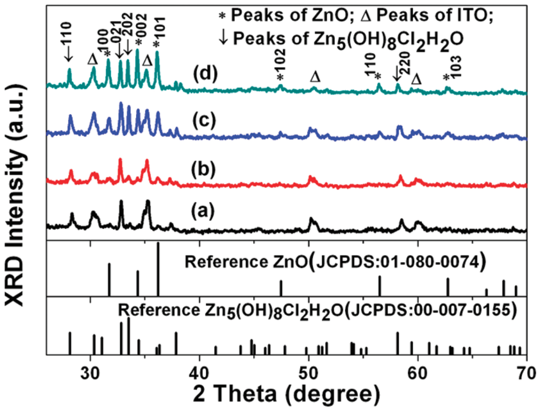

Figure 10. XRD patterns of $ZnO/Zn_5(OH)_8Cl_2H_2O$ nanosheet arrays electrodeposited at different temperatures (T): (a) 50, (b) 60, (c) 70, and (d) 80 °C.

According to eq 7, after annealing in the air at high temperature, there would be a weight loss in $ZnO/Zn_5(OH)_8Cl_2H_2O$ nanodeposits due to decomposition of $Zn_5(OH)_8Cl_2H_2O$. Thus the variation in composition of $ZnO/Zn_5(OH)_8Cl_2H_2O$ nanosheets synthesized at different temperatures can be further confirmed by the thermal decomposition behavior of the samples. The TGA curve shown in Figure 11a indicates that the weight loss of the $ZnO/Zn_5(OH)_8Cl_2H_2O$ nanosheets electrodeposited at 50 °C is about 25%, which agrees well to the theoretical value of $Zn_5(OH)_8Cl_2H_2O$ (26.27%), suggesting that the products are basically composed of $Zn_5(OH)_8Cl_2H_2O$. Increasing the deposition temperature gives rise to a decrease in weight loss (Figure 11b−d), which can be ascribed to the increased amount of ZnO in the synthesized nanodeposits. For the $ZnO/Zn_5(OH)_8Cl_2H_2O$ nanosheets electrodeposited at 80 °C, the weight loss is just half as much as that of the nanosheets electrodeposited at 50 °C (Figure 11d), implying the large amount of ZnO formed at high temperature, which is consistent with the XRD analysis shown in Figure 10d.

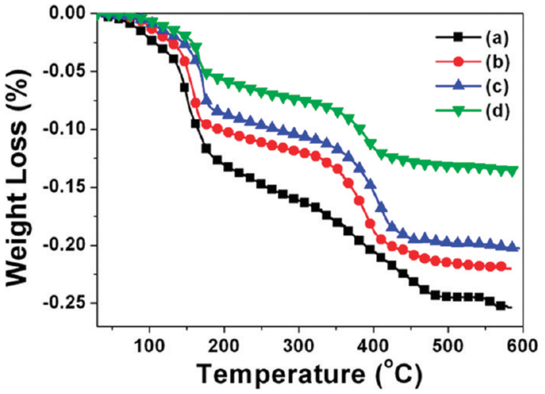

Figure 11. TGA curves of $ZnO/Zn_5(OH)_8Cl_2H_2O$ nanosheets electrodeposited at different temperatures (T): (a) 50, (b) 60, (c) 70, and (d) 80 °C.

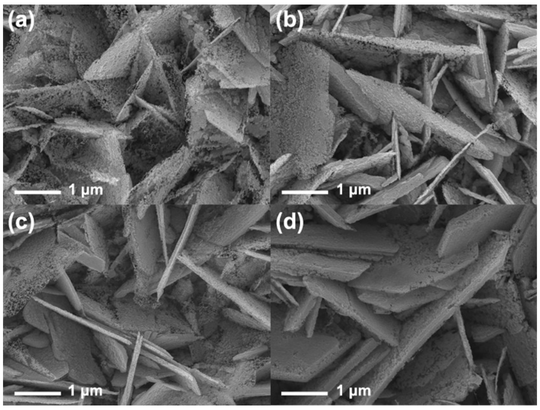

Figure 12. SEM images of ZnO nanosheets obtained by annealing the $ZnO/Zn_5(OH)_8Cl_2H_2O$ nanosheets electrodeposited at different temperatures (T): (a) 50, (b) 60, (c) 70, and (d) 80 °C.

Figure 12 presents the SEM images of ZnO nanosheet arrays obtained by annealing $ZnO/Zn_5(OH)_8Cl_2H_2O$ nanosheet arrays that are synthesized at different temperatures (Figure 9). It can be seen that the surface of the ZnO nanosheets electrodeposited at low temperature appears to be rougher than that of the nanosheets electrodeposited at high temperature. This can be ascribed to the different weight loss of $ZnO/Zn_5(OH)_8Cl_2H_2O$ nanosheets after annealing treatment (Figure 11), which determines the amount of asperities formed on the surface of the ZnO nanosheets (Figure 12). The difference in the amount of asperities can thus determine the density of the secondary ZnO nanorods in the synthesized hierarchical nanostructures, which is presented in Figure 13. When the growth temperature of the primary $ZnO/Zn_5(OH)_8Cl_2H_2O$ nanosheets is lower than 60 °C, the as-synthesized secondary nanorods almost merge with one another due to the high growth density (Figure 13a and b), which is caused by the large amount of active centers (asperities) on the primary nanosheet surface (Figure 12a and b). With the temperature of the first-step deposition process increasing to 70 °C, the amount of independent secondary nanorods increases (Figure 13c), mainly because of the decreased amount of active centers (asperities) (Figure 12c). However, as the growth temperature of the primary nanosheets further increases to 80 °C, there are lots of primary nanosheets which are not

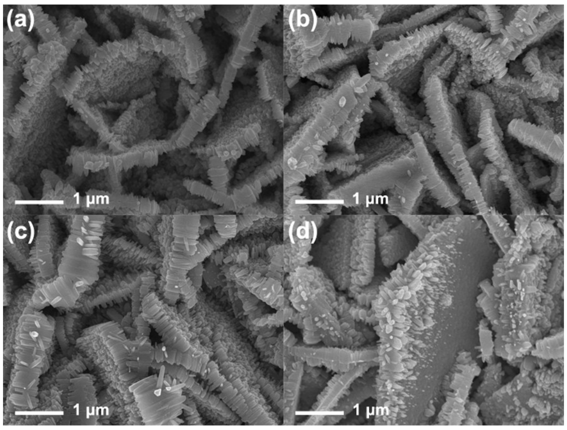

Figure 13. SEM images of hierarchical ZnO nanorod-nanosheet structures synthesized by two-step deposition process with different first-step deposition temperatures (T_1): (a) 50, (b) 60, (c) 70, and (d) 80 °C. Other electrodeposition conditions, first-step deposition: $C_{Zn}{}^{2+}$ = 0.05 M ($Zn(NO_3)_2$), E_1 = −1.0 V, t_1 = 1 h; second-step deposition: T_2 = 80 °C, $C_{Zn}{}^{2+}$ = 1 mM ($ZnCl_2$), E_2 = −1.0 V, t_2 = 1 h.

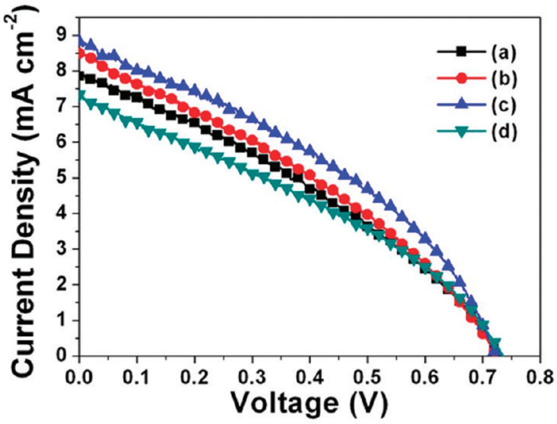

Figure 14. Photocurrent−voltage curves of DSSCs based on ZnO nanorod-nanosheet structures synthesized by two-step deposition process with different first-step deposition temperatures (T_1): (a) 50, (b) 60, (c) 70, and (d) 80 °C.

Table 2. Photovoltaic Properties of DSSCs Based on Hierarchical ZnO Nanorod-Nanosheet Structures Synthesized by Two-Step Deposition Process with Different First-Step Deposition Temperatures[a]

ZnO DSSCs	J_{sc} (mA cm^{-2})	V_{oc} (V)	FF	η (%)	amount of adsorbed dye (× 10^{-8} mol cm^{-2})
sample a	7.89	0.73	0.34	1.92	3.63
sample b	8.56	0.72	0.33	2.05	3.76
sample c	8.82	0.72	0.37	2.37	4.11
sample d	7.33	0.73	0.34	1.81	3.54

[a] The error is ±5%. Growth temperatures of the first-step deposition process (T_1): sample a, 50 °C, sample b, 60 °C; sample c, 70 °C; and sample d, 80 °C. Other electrodeposition conditions, first-step deposition: $C_{Zn}{}^{2+}$ = 0.05 M ($Zn(NO_3)_2$), E_1 = −1.0 V, t_1 = 1 h; second-step deposition: T_2 = 80 °C, $C_{Zn}{}^{2+}$ = 1 mM ($ZnCl_2$), E_2 = −1.0 V, t_2 = 1 h.

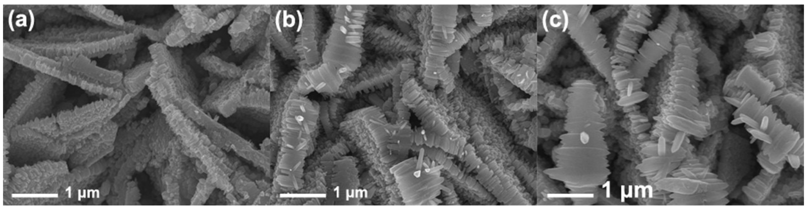

Figure 15. SEM images of ZnO nanorod-nanosheet structures synthesized by two-step deposition process with different second-step deposition times (t_2): (a) 0.5, (b) 1, and (c) 2 h. Other electrodeposition conditions, first-step deposition: $T_1 = 70$ °C, $C_{Zn^{2+}} = 0.05$ M ($Zn(NO_3)_2$), $E_1 = -1.0$ V, $t_1 = 1$ h; second-step deposition: $T_2 = 80$ °C, $C_{Zn^{2+}} = 1$ mM ($ZnCl_2$), $E_2 = -1.0$ V.

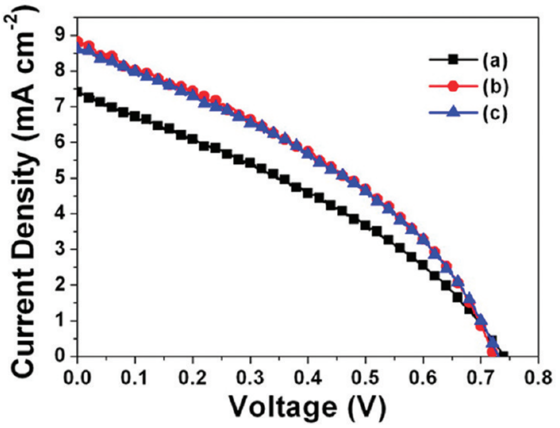

Figure 16. Photocurrent−voltage curves of DSSCs based on hierarchical ZnO nanorod-nanosheet structures synthesized by two-step deposition process with different second-step deposition times (t_2): (a) 0.5, (b) 1, and (c) 2 h.

Table 3. Photovoltaic Properties of DSSCs Based on Hierarchical ZnO Nanorod-Nanosheet Structures Synthesized by Two-Step Deposition Process with Different Second-Step Deposition Times[a]

ZnO DSSCs	J_{sc} (mA cm^{-2})	V_{oc} (V)	FF	η (%)	amount of adsorbed dye ($\times 10^{-8}$ mol cm^{-2})
sample a	7.43	0.74	0.34	1.89	3.65
sample b	8.82	0.72	0.37	2.37	4.11
sample c	8.68	0.73	0.37	2.32	3.98

[a] The error is ±5%. Growth times of the second-step deposition process (t_2): sample a, 0.5 h; sample b, 1 h; and sample c, 2 h. Other electrodeposition conditions, first-step deposition: $T_1 = 70$ °C, $C_{Zn^{2+}} = 0.05$ M ($Zn(NO_3)_2$), $E_1 = -1.0$ V, $t_1 = 1$ h; second-step deposition: $T_2 = 80$ °C, $C_{Zn^{2+}} = 1$ mM ($ZnCl_2$), $E_2 = -1.0$ V.

covered by secondary nanorods shown in hierarchical nanostructure (Figure 13d). This can be attributed to the large amount of ZnO formed in primary ZnO/$Zn_5(OH)_8Cl_2H_2O$ nanosheets. For the ZnO/$Zn_5(OH)_8Cl_2H_2O$ nanosheets that are mainly composed of ZnO, few asperities can be formed after annealing treatment because of the low weight loss (Figure 11d), as shown in Figure 12d. Thus few ZnO nanorods can be produced during the second-step deposition process, leading to much area of primary nanosheets exposed in the synthesized hierarchical nanostructure.

The photovoltaic properties of the DSSCs constructed with the hierarchical ZnO nanorod-nanosheet structures whose SEM images are shown in Figure 13 vary dramatically, which is presented in Figure 14 and Table 2. The variation might be ascribed to the difference in the morphology of the secondary nanorods, which can therefore influence the internal surface area of the photoelectrodes. Although the introduction of secondary nanorods can increase the internal surface area of the hierarchical nanostructure photoelectrode when compared to the nanosheet one, the increasing extents are of difference for the nanostructures with different densities of the secondary nanorods (Figure 13). From Figure 13a and b, it can be seen that the increase in internal surface area is limited due to the large amount of secondary nanorods merging with one another. Thus the dye loading of the photoelectrode is restricted to the low level ($3.63-3.76 \times 10^{-8}$ mol cm^{-2}), leading to the low short-circuit current densities (Figure 14a and b) and hence the low power conversion efficiencies (1.92% and 2.05%). Because of the relatively large internal surface area, which is mainly caused by the increased amount of independent secondary nanorods in hierarchical nanorod-nanosheet structures (Figure 13c), the power conversion efficiency of the DSSC increases to 2.37% (Figure 14c and sample c in Table 2). However, for the photoelectrode whose SEM image is shown in Figure 13d, the increase in internal surface area is considerably restrained due to the lack of secondary nanorods in hierarchical nanostructure, which results in the low dye loading (3.54×10^{-8} mol cm^{-2}) and hence the low short-circuit current density (7.33 mA cm^{-2}) (Figure 14d sample d in Table 2). Consequently, the power conversion efficiency of the DSSC is reduced to 1.81%.

3.3. Influence of the Second-Step Deposition Time on the Morphology of the Synthesized Hierarchical Nanostructure Photoelectrodes and Their Photovoltaic Properties. To further investigate the influence of the morphology of secondary ZnO nanorods on the DSSC performance, second-step deposition time was adjusted to 0.5, 1, and 2 h respectively while other parameters of the two-step deposition process were kept constant. The resulting SEM images are presented in Figure 15. It can be seen from Figure 15a and b that, with increasing this parameter from 0.5 to 1 h, there is an obvious increase in the length of the secondary nanorods, which can enlarge the internal surface area of the hierarchical nanostructure film and hence enhancing the dye loading of the photoelectrode. As a result, improvement in short-circuit current density is achieved (Figure 16), leading to the increase in power conversion efficiency (from 1.89 to 2.37%) (sample a and b in Table 3). However, as the time of the second-step deposition process increases to 2 h, the increase in the length of the secondary nanorods is not obvious, whereas lots of the secondary nanorods merge with one another due to the lateral growth of ZnO nanorods (Figure 15c). This variation in geometric size of the

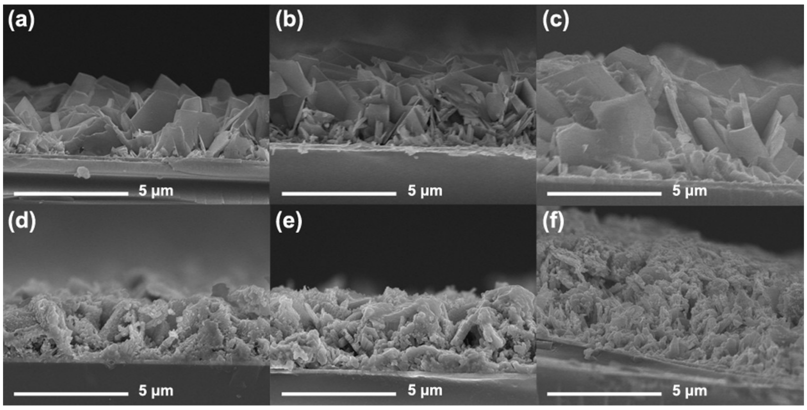

Figure 17. Cross-sectional SEM images of $ZnO/Zn_5(OH)_8Cl_2H_2O$ nanosheet arrays with different growth times (t): (a) 1, (b) 2, (c) 4 h, and hierarchical ZnO nanorod-nanosheet structures synthesized by two-step deposition process with different first-step deposition times (t_1): (d) 1, (e) 2, (f) 4 h. Other electrodeposition conditions of the $ZnO/Zn_5(OH)_8Cl_2H_2O$ nanosheet arrays: $T = 70$ °C, $C_{Zn}^{2+} = 0.05$ M ($Zn(NO_3)_2$), $E = -1.0$ V, Other electrodeposition conditions of the hierarchical ZnO nanorod-nanosheet structures, first-step deposition: $T_1 = 70$ °C, $C_{Zn}^{2+} = 0.05$ M ($Zn(NO_3)_2$), $E_1 = -1.0$ V; second-step deposition: $T_2 = 80$ °C, $C_{Zn}^{2+} = 1$ mM ($ZnCl_2$), $E_2 = -1.0$ V, $t_2 = 1$ h.

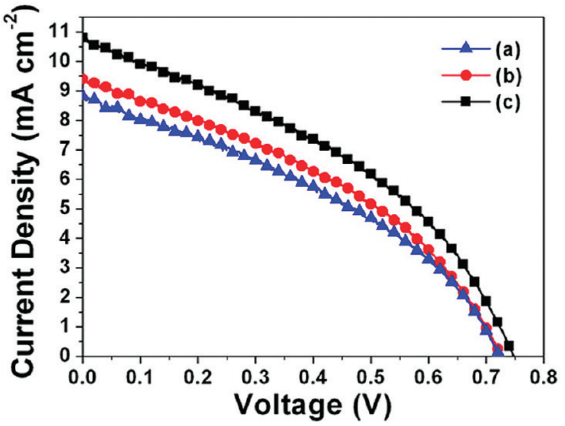

Figure 18. Photocurrent–voltage curves of DSSCs based on ZnO nanorod-nanosheet structures with different film thicknesses.

Table 4. Photovoltaic Properties of DSSCs Based on ZnO Nanorod-Nanosheet Structures with Different Film Thicknesses[a]

ZnO DSSCs	J_{sc} (mA cm^{-2})	V_{oc} (V)	FF	η (%)	amount of adsorbed dye (× 10^{-8} mol cm^{-2})
sample a	8.82	0.72	0.37	2.37	4.11
sample b	9.41	0.72	0.38	2.62	4.54
sample c	10.85	0.74	0.38	3.12	5.46

[a] The error is ±5%. Growth times of the first-step deposition process (t_1): sample a, 1 h; sample b, 2 h; and sample c, 4 h. Other electrodeposition conditions, first-step deposition: $T_1 = 70$ °C, $C_{Zn}^{2+} =$ 0.05 M ($Zn(NO_3)_2$), $E_1 = -1.0$ V; second-step deposition: $T_2 = 80$ °C, $C_{Zn}^{2+} = 1$ mM ($ZnCl_2$), $E_2 = -1.0$ V, $t_2 = 1$ h.

secondary nanorods might cause the decrease in internal surface area of the photoelectrode and thus the slight decline in power conversion efficiency (2.32%), which is demonstrated in Figure 16c and Table 3 (sample c).

3.4. Influence of the First-Step Deposition Time on the Morphology of the Synthesized Hierarchical Nanostructure Photoelectrodes and Their Photovoltaic Properties. The influence of the film thickness of hierarchical ZnO nanostructures on DSSC performance was investigated by adjusting the time of the first-step deposition process. The cross-sectional SEM images of the primary $ZnO/Zn_5(OH)_8Cl_2H_2O$ nanosheet arrays synthesized at deposition time of 1, 2, and 4 h are presented in Figure 17a–c, whereas Figure 17d–f show the corresponding cross-sectional SEM images of the hierarchical ZnO nanorod-nanosheet structures synthesized by two-step deposition process with different first-step deposition times (1, 2, and 4 h). Figure 17 indicates that the film thickness of the hierarchical nanostructure is mainly determined by the time of the first-step deposition process. Increasing the first-step deposition time gives rise to an increase in film thickness, from 3–4 μm at 1 h to 6–7 μm at 4 h, which can consequently influence the DSSC performance, as shown in Figure 18 and Table 4. Because of the enlargement of internal surface area, caused by the increase in film thickness, better dye loading of the hierarchical nanostructure photoelectrode is achieved, which accordingly increases the short-current density and the power conversion efficiency of the corresponding DSSC. Furthermore, by using the hierarchical ZnO nanorod-nanosheet structures with thickness of ~7 μm as photoelectrode (Figure 17f), the DSSC with power conversion efficiency of 3.12% and open circuit voltage as high as 0.74 V is achieved successfully.

4. CONCLUSION

In summary, we present a simple two-step electrodeposition process to synthesize hierarchical ZnO nanorod-nanosheet structures on ITO substrate. It has been demonstrated that the presence of $Zn_5(OH)_8Cl_2H_2O$ in the primary nanosheets, which can allow the formation of active centers for ZnO nucleation by annealing treatment, is crucial for synthesizing the hierarchical nanorod-nanosheet structures. The DSSC based on the synthesized hierarchical nanostructures exhibits improved device performance compared to the DSSC consisting of bare ZnO nanosheet arrays, which is mainly attributed to the enlargement of internal surface area within the photoelectrode, caused by the introduction of the secondary ZnO nanorods. Moreover, the morphology of the hierarchical nanostructure can be changed by adjusting the preparation conditions of the two-step deposition process, and the DSSCs consisting of the hierarchical ZnO nanostructures with different geometric sizes exhibit different photovoltaic properties. By fine-turning the preparation conditions, hierarchical ZnO nanostructure DSSC with power conversion efficiency of 3.12% and open circuit voltage of 0.74 V is successfully produced.

AUTHOR INFORMATION

Corresponding Author

*Tel.: +86 10 80529083. Fax: +86 10 82529010. E-mail: xidong@pku.edu.cn (X. Wang).

ACKNOWLEDGMENT

The work is supported by the National Science Foundation of China (50772004, 51074009) and the National Basic Research Program of China (973 Program:2007CB613608).

REFERENCES

(1) Oregan, B.; Gratzel, M. *Nature* **1991**, *353*, 737–740.

(2) Gratzel, M. *Nature* **2001**, *414*, 338–344.

(3) Chiba, Y.; Islam, A.; Watanabe, Y.; Komiya, R.; Koide, N.; Han, L. Y. *Jpn. J. Appl. Phys.* **2006**, *45*, L638–L640.

(4) Gao, F.; Wang, Y.; Shi, D.; Zhang, J.; Wang, M. K.; Jing, X. Y.; Humphry-Baker, R.; Wang, P.; Zakeeruddin, S. M.; Gratzel, M. *J. Am. Chem. Soc.* **2008**, *130*, 10720–10728.

(5) Frank, A. J.; Kopidakis, N.; van de Lagemaat, J. *Coord. Chem. Rev.* **2004**, *248*, 1165–1179.

(6) Zhang, Q. F.; Dandeneau, C. S.; Zhou, X. Y.; Cao, G. Z. *Adv. Mater.* **2009**, *21*, 4087–4108.

(7) Nissfolk, J.; Fredin, K.; Hagfeldt, A.; Boschloo, G. *J. Phys. Chem. B* **2006**, *110*, 17715–17718.

(8) Gratzel, M. *Inorg. Chem.* **2005**, *44*, 6841–6851.

(9) Gratzel, M. *J. Photochem. Photobiol. A* **2004**, *164*, 3–14.

(10) Law, M.; Greene, L. E.; Johnson, J. C.; Saykally, R.; Yang, P. D. *Nat. Mater.* **2005**, *4*, 455–459.

(11) Martinson, A. B. F.; Elam, J. W.; Hupp, J. T.; Pellin, M. J. *Nano Lett.* **2007**, *7*, 2183–2187.

(12) Ozgur, U.; Alivov, Y. I.; Liu, C.; Teke, A.; Reshchikov, M. A.; Dogan, S.; Avrutin, V.; Cho, S. J.; Morkoc, H. *J. Appl. Phys.* **2005**, *98*, 041301.

(13) Tang, H.; Prasad, K.; Sanjines, R.; Schmid, P. E.; Levy, F. *J. Appl. Phys.* **1994**, *75*, 2042–2047.

(14) Bae, H. S.; Yoon, M. H.; Kim, J. H.; Im, S. *Appl. Phys. Lett.* **2003**, *83*, 5313–5315.

(15) Baxter, J. B.; Aydil, E. S. *Sol. Energer Mater. Sol. Cells* **2006**, *90*, 607–622.

(16) Suh, D. I.; Lee, S. Y.; Kim, T. H.; Chun, J. M.; Suh, E. K.; Yang, O. B.; Lee, S. K. *Chem. Phys. Lett.* **2007**, *442*, 348–353.

(17) Lee, C. H.; Chiu, W. H.; Lee, K. M.; Yen, W. H.; Lin, H. F.; Hsieh, W. F.; Wu, J. M. *Electrochim. Acta* **2010**, *55*, 8422–8429.

(18) Jiang, C. Y.; Sun, X. W.; Lo, G. Q.; Kwong, D. L.; Wang, J. X. *Appl. Phys. Lett.* **2007**, *90*, 263501.

(19) Xu, F.; Dai, M.; Lu, Y. N.; Sun, L. T. *J. Phys. Chem. C* **2010**, *114*, 2776–2782.

(20) Cheng, H. M.; Chiu, W. H.; Lee, C. H.; Tsai, S. Y.; Hsieh, W. F. *J. Phys. Chem. C* **2008**, *112*, 16359–16364.

(21) Li, Y. B.; Zheng, M. J.; Ma, L.; Zhong, M.; Shen, W. Z. *Inorg. Chem.* **2008**, *47*, 3140–3143.

(22) Lao, J. Y.; Wen, J. G.; Ren, Z. F. *Nano Lett.* **2002**, *2*, 1287–1291.

(23) Gao, P. X.; Wang, Z. L. *J. Phys. Chem. B* **2002**, *106*, 12653–12658.

(24) Lao, J. Y.; Huang, J. Y.; Wang, D. Z.; Ren, Z. F. *Nano Lett.* **2003**, *3*, 235–238.

(25) Zhang, T. R.; Dong, W. J.; Keeter-Brewer, M.; Konar, S.; Njabon, R. N.; Tian, Z. R. *J. Am. Chem. Soc.* **2006**, *128*, 10960–10968.

(26) Xu, L. F.; Chen, Q. W.; Xu, D. S. *J. Phys. Chem. C* **2007**, *111*, 11560–11565.

(27) Peulon, S.; Lincot, D. *J. Electrochem. Soc.* **1998**, *145*, 864–874.

(28) Izaki, M.; Omi, T. *Appl. Phys. Lett.* **1996**, *68*, 2439–2440.

(29) Pauporte, T.; Lincot, D. *J. Electrochem. Soc.* **2001**, *148*, C310–C314.

(30) Pradhan, D.; Leung, K. T. *Langmuir* **2008**, *24*, 9707–9716.

(31) Tena-Zaera, R.; Elias, J.; Wang, G.; Levy-Clement, C. *J. Phys. Chem. C* **2007**, *111*, 16706–16711.

(32) Elias, J.; Tena-Zaera, R.; Levy-Clement, C. *J. Phys. Chem. C* **2008**, *112*, 5736–5741.

(33) Pradhan, D.; Kumar, M.; Ando, Y.; Leung, K. T. *ACS Appl. Mater. Interface* **2009**, *1*, 789–796.

(34) Pauporte, T.; Bataille, G.; Joulaud, L.; Vermersch, F. J. *J. Phys. Chem. C* **2010**, *114*, 194–202.

(35) El Belghiti, H.; Pauporte, T.; Lincot, D. *Phys. Stat. Solidi A* **2008**, *205*, 2360–2364.

(36) Pradhan, D.; Leung, K. T. *J. Phys. Chem. C* **2008**, *112*, 1357–1364.

(37) Wang, P.; Klein, C.; Humphry-Baker, R.; Zakeeruddin, S. M.; Gratzel, M. *J. Am. Chem. Soc.* **2005**, *127*, 808–809.

(38) Wang, Z. S.; Kawauchi, H.; Kashima, T.; Arakawa, H. *Coord. Chem. Rev.* **2004**, *248*, 1381–1389.

(39) Futsuhara, M.; Yoshioka, K.; Takai, O. *Thin Solid Films* **1998**, *317*, 322–325.

(40) Liu, B.; Zeng, H. C. *J. Am. Chem. Soc.* **2004**, *126*, 16744–16746.

(41) Bar, M.; Reichardt, J.; Sieber, I.; Grimm, A.; Kotschau, I.; Lauermann, I.; Sokoll, S.; Lux-Steiner, M. C.; Fischer, C. H.; Niesen, T. P. *J. Appl. Phys.* **2006**, *100*, 023710.

(42) Fortunato, E. M. C.; Pereira, L. M. N.; Barquinha, P. M. C.; do Rego, A. M. B.; Goncalves, G.; Vila, A.; Morante, J. R.; Martins, R. F. P. *Appl. Phys. Lett.* **2008**, *92*, 222103.

(43) Gaarenstroom, S. W.; Winograd, N. *J. Chem. Phys.* **1977**, *67*, 3500–3506.

(44) Strohmeier, B. R.; Hercules, D. M. *J. Catal.* **1984**, *86*, 266–279.